

# Detection of Satellite Remnants in the Galactic Halo with Gaia – II. A modified Great Circle Cell Method

C. Mateu,<sup>1\*</sup> G. Bruzual,<sup>1</sup> L. Aguilar,<sup>2</sup> A.G.A Brown,<sup>3</sup>  
O. Valenzuela,<sup>4</sup> L. Carigi,<sup>4</sup> F. Hernández,<sup>1</sup> H. Velázquez<sup>2</sup>

<sup>1</sup>*Centro de Investigaciones de Astronomía, AP 264, Mérida 5101-A, Venezuela*

<sup>2</sup>*Instituto de Astronomía, UNAM, Apartado Postal 877, 22860 Ensenada, B.C., México*

<sup>3</sup>*Sterrewacht Leiden, Leiden University, PO Box 9513, 2300 RA Leiden, the Netherlands*

<sup>4</sup>*Instituto de Astronomía, UNAM, Apartado Postal 70-264, 04510 México, D.F., México*

13 January 2013

## ABSTRACT

We propose an extension of the GC3 streamer finding method of Johnston et al. (1996) that can be applied to the future Gaia database. The original method looks for streamers along great circles in the sky, our extension adds the kinematical restriction that velocity vectors should also be constrained to lie along these great circles, as seen by a Galactocentric observer. We show how to use these combined criteria starting from heliocentric observables. We test it by using the mock Gaia catalogue of Brown et al. (2005), which includes a realistic Galactic background and observational errors, but with the addition of detailed star formation histories for the simulated satellites. We investigate its success rate as a function of initial satellite luminosity, star formation history and orbit. We find that the inclusion of the kinematical restriction vastly enhances the contrast between a streamer and the background, even in the presence of observational errors, provided we use only data with good astrometric quality (fractional errors of 30 per cent or better). The global nature of the method diminishes the erasing effect of phase mixing and permits the recovery of merger events of reasonable dynamical age. Satellites with a star formation history different to that of the Galactic background are also better isolated. We find that satellites in the range of  $10^8 - 10^9 L_{\odot}$  can be recovered even for events as old as  $\sim 10$  Gyr. Even satellites with  $4 - 5 \times 10^7 L_{\odot}$  can be recovered for certain combinations of dynamical ages and orbits.

## 1 INTRODUCTION

The  $\Lambda$  cold dark matter ( $\Lambda$ CDM) hierarchical paradigm is the best model we have to explain the large-scale structure of the Universe (Springel, Frenk & White 2006; Spergel et al. 2007; Klypin, Trujillo-Gomez & Primack 2010). In recent years, it has proved to successfully reproduce a number of observational measurements (e.g. spatial and colour-magnitude distributions) for galaxies observed in the local Universe and at higher redshift (for recent reviews see Baugh 2006; Avila-Reese 2006). In spite of the encouraging progress on the large scale, at galactic and subgalactic scales, the success of the model has not been convincingly demonstrated as yet, and a number of issues remain subject of a lively debate in the astronomical community. Examples of these are the core-cusp issue (de Blok 2010; Governato et al. 2010; Puglielli, Widrow & Courteau 2010; Valenzuela et al. 2007; Gentile et al. 2004), the

missing satellites problem (Klypin et al. 1999; Moore et al. 1999; Kravtsov 2010), the angular momentum problem (Abadi et al. 2003; Governato et al. 2004; Okamoto et al. 2005; Governato et al. 2007), or the Downsizing-Specific Star Formation Rate relation for dwarf galaxies (Colin et al. 2009; Firmani, Avila-Reese & Rodriguez-Puebla 2009; Bauer et al. 2005).

Another powerful test for the  $\Lambda$ CDM scenario at subgalactic scales, may be provided by galaxy halos, in particular by the Milky Way (MW) stellar halo. If the Galaxy was assembled in a hierarchical way, there must be fossil signatures in the phase space distribution of halo stars and also in the Galactic disc, although kinematic features in the latter may have multiple origins (Antoja et al. 2009; Minchev et al. 2009; Gómez & Helmi 2010). Theoretically, the origin and structure of the stellar halo have been studied by several authors using a variety of techniques (for a review, see Helmi 2008). These include cosmological numerical simulations with and without baryonic physics (Zolotov et al. 2009; Diemand, Madau & Moore 2005; Abadi et al. 2003)

\* cmateu@cida.vc

and phenomenological modelling of the evolution of baryons inside haloes, usually in combination with N-body simulations that provide the dynamical history of the system (Bullock & Johnston 2005; Cooper et al. 2009). Historically, chemical and kinematic information was used as a basis to formulate the first galaxy formation models. In their classical paper, Eggen, Lynden-Bell & Sandage (1962) suggested a rapid radial collapse that later continued to form the stellar disc. About a decade later, Searle & Zinn (1978) formulated the hypothesis that the stellar halo formed over a longer time-scale, through the agglomeration of many subgalactic ‘fragments’ that may be similar to the surviving dwarf spheroidal galaxies observed today as satellites of the Milky Way. The Searle & Zinn (1978) scenario and several observational results are in qualitative agreement with expectations from the  $\Lambda$ CDM model (De Lucia & Helmi 2008). However, the observed abundance pattern (Tolstoy et al. 2009) seems to exclude the possibility that a significant contribution to the stellar halo comes from disrupted satellites similar to the present-day dSphs (Bullock & Johnston 2005; Robertson et al. 2005; Font et al. 2006).

Over the next decade, a number of astrometric and spectroscopic surveys will provide accurate spatial, kinematic and chemical information for a large number of stars e.g. the Gaia satellite (Lindegren et al. 2008); the Radial Velocity Experiment-RAVE (Steinmetz et al. 2006) and the Sloan Extension for Galactic Understanding and Exploration- SEGUE (Yanny et al. 2009). This vast fossil records will provide important advances in our understanding of the sequence of events which led to the formation of our Galaxy (Freeman & Bland-Hawthorn 2002).

It is critical to design efficient strategies in order to extract valuable dynamical information from the plethora of upcoming observations. The task is not a trivial one. It is not clear which is the optimal strategy, or in which space substructure can be best located. Natural diagnostics like integrals of motion variables may be hampered by the finite accuracy of surveys (Helmi & White 1999; Helmi & de Zeeuw 2000). Recently, action-angle variables have shown to provide a promising avenue (Gómez & Helmi 2010). In addition, Font et al. (2006) showed the usefulness of chemical information in identifying the relics of merger events.

In the present work we continue the study initiated in Brown, Velázquez & Aguilar (2005, hereafter B05), to revisit the possibilities of extracting reliable information about past merger events in the halo of our Galaxy in the upcoming Gaia database. In the previous study, we developed the numerical machinery to build ‘mock’ Gaia catalogues that include merger events from  $N$ -body simulations against a realistic smooth Galactic background. Spatial, velocity and photometric information from a Galaxy model with three separate components (bulge, disc and halo) was used. Sampling issues were tackled, like the variation in probing depth of the satellite stellar luminosity function, as a function of position along a tidal streamer. A realistic model for Gaia errors was included too. With the resulting catalogue, a re-examination of the integral-space method of Helmi & de Zeeuw (2000) was done and it was concluded that, although promising, in real practice observational errors and the presence of an overwhelming Galactic background can compromise the efficiency of this method and great care in its use must be exercised. It is clear that we must use as many search tech-

niques as possible, preferably those that include as much observationally available information as possible.

Following this path, we have decided to investigate now the ‘Great Circle Cell Count’ (GC3) method proposed by Johnston, Hernquist & Bolte (1996), in order to find a way to increase its efficiency. We propose an extension to this method, that we dubbed mGC3 (‘modified GC3’), which adds kinematical information to the original method, in order to detect substructures in the MW stellar halo. We have used the mock Gaia catalogue of B05, with the further improvement of a more detailed modeling of the simulated photometry of the satellites, so they now reflect specific histories of star formation. The expected Gaia measurement errors were simulated as a function of magnitude, colour, and sky position of the stars, as described in appendix A of B05. The values of the expected errors were updated to the latest predictions of the scientific performance of Gaia. The latter can be found at <http://www.rssd.esa.int/gaia> under the ‘Science performance’ entry. Compared to the performance predictions used in B05 the current astrometric error estimates are larger by a factor of two. We specifically assess the effect of the predicted Gaia observational errors on the ability of GC3/mGC3 strategies to find simulated satellite remnants. We also study the effects on recovery efficiency when varying the orbit, luminosity and star formation history of the satellites.

In section 2, we present a brief outlook on the problem of identifying past merger events and review the original GC3 method. Some specific examples are shown to illustrate how it works. In section 3 the mGC3 extension is introduced. The basic concept, as well as a practical way to implement it, are discussed. In section 4, we evaluate the applicability of the mGC3 method using the mock catalogue of B05. We also describe the way in which we have included various star formation histories for the satellites using and adaptation of the stellar population synthesis software of Bruzual & Charlot (2003). In section 5, we study in detail the efficiency of the mGC3 method in identifying past merger events, as a function of satellite orbit, luminosity and star formation history. Our conclusions are presented in section 6.

## 2 THE GREAT CIRCLE CELL COUNT METHOD

Current computer capabilities allow us to explore the formation and evolution of stellar streams under a variety of conditions, such as different orbits and underlying potentials, via N-body simulations. The understanding of common properties of stellar streams, as well as their time evolution, are key to develop effective identification techniques. This goes hand in hand with the observational developments that will allow the practical application of such techniques to real data.

Key properties that determine the dynamical structure and evolution of stellar streams, which in turn can be used in their identification, are the integrals of motion: the total energy  $E$ , if the Galactic potential is stationary; the total angular momentum  $L$ , if the potential has spherical symmetry; and its projection  $L_z$ , if the potential has axial symmetry.

The existence of these conserved quantities leads naturally to the search of streams as entities in integrals of motion space, as proposed by Helmi & de Zeeuw (2000). This

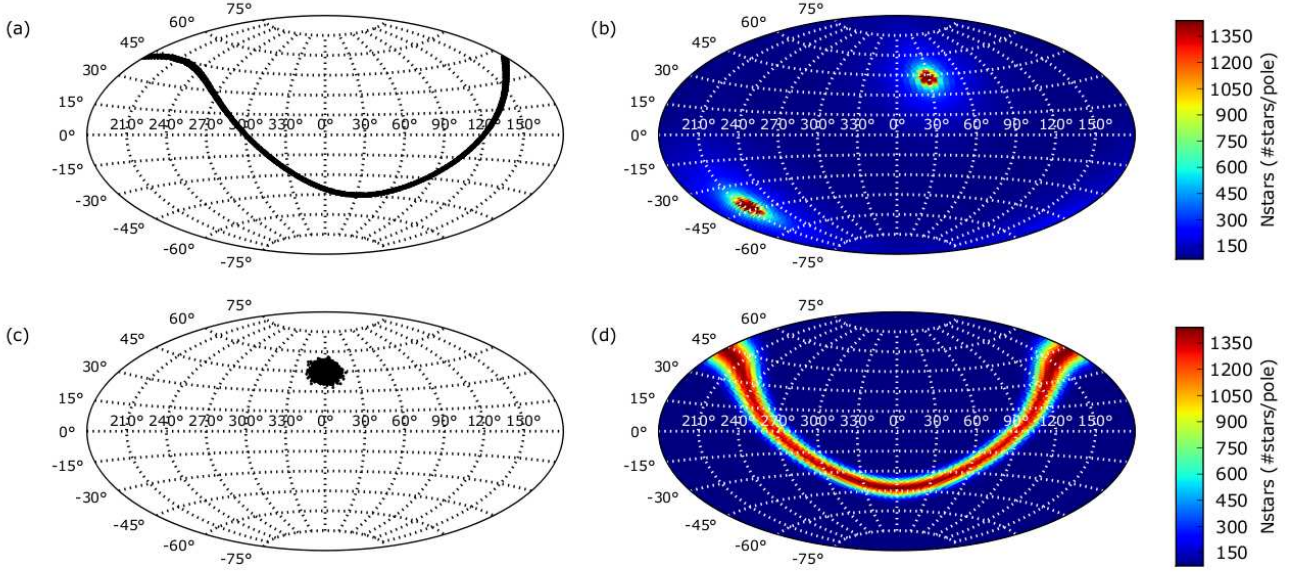


**Figure 1.** Illustration of spatial and corresponding GC3 pole count maps of simple stellar distributions, shown in Aitoff projections. (a) Spatial distribution of  $9 \times 10^3$  simulated stars in a planar circular orbit, with an inclination of  $45^\circ$  with respect to the Galactic Plane. (b) GC3 pole count map of stars shown in (a). (c) Spatial distribution of  $9 \times 10^3$  simulated stars with a localized gaussian distribution. (d) GC3 pole count map of stars shown in (d).

technique requires the computation of the conserved quantities in terms of observed ones, like  $(l, b, \varpi, v_r, \mu_l, \mu_b)$ , the Galactic latitude and longitude, parallax, radial velocity and proper motions, respectively. These computations involve non-linear transformations resulting also in non-linear error propagation which, as B05 show, lead to systematic errors in  $E, L, L_z$  as their expectation values do not equal their true values once the observational errors are introduced. Furthermore, the spread of errors is greatly magnified, as shown there. Additionally, the computation of the total energy  $E$  requires an assumption about the underlying potential, which is an unknown and thus introduces another source of error. It is clear that, although powerful in theory, the integrals of motion technique has its limitations when applied to real data. It is thus convenient to look for additional search techniques that may complement it.

A different approach in the identification of tidal streams is the GC3 method proposed by Johnston et al. (1996), which uses the conservation of the total angular momentum in a geometrical way. It relies on the fact that the orbits of stars in a stream in a spherical potential will be confined to a plane that contains the potential center. As seen from the Galactic center, this plane is a great circle on the sky. In the more general case of an axisymmetric Galactic potential, the orbital plane precesses around the axis of symmetry of the system. This will result in the stream being approximately confined to a plane with a finite thickness, which in turn corresponds to a great circle of finite width. A further complication arises from the fact that we are not at the Galactic center, which spoils to some degree the great circle effect, particularly for streamers whose orbits lie within, or near the Sun's orbit.

The practical implementation of the GC3 method begins by laying down a grid on the celestial sphere. Each grid point is then associated to a unit vector  $\hat{L}$  (pole vector) that points from the observer to the grid point. All stars on the sky that lie on a band defined by the great circle in the plane orthogonal to the pole vector, are associated to this pole or grid point, the angular width of the band being specified independently. The number of stars within this band are assigned to the corresponding pole. The counts associated to every grid point in the mesh thus define a *pole count map*. Significant maxima in this pole count map are then accepted as possible streamers. Because of the geometry, the pole vector will be parallel to the angular momentum of all stars in the band whose velocity vector also lies in the orbital plane defined by the great circle. This latter property will be exploited later on, when we introduce the extended GC3 method.

$$|\hat{L} \cdot \hat{r}| \leq \delta_r \quad (1)$$

where  $\hat{r}$  is a unit vector pointing to the star and  $\delta_r = \sin \delta \theta$  is the tolerance which allows for the width  $\delta \theta$  of each great circle associated to a cell (see Sec. 3.1 and Fig. 7 in Johnston et al. 1996). The distribution of pole counts is then represented in a map of the celestial sphere.

We illustrate the pole count maps for two simple *simulated* stellar distributions in Fig. 1a-d, in order to explain their morphology. The spatial distribution of  $9 \times 10^3$  stars in a circular orbit with a  $45^\circ$  inclination is shown in Fig. 1a and the corresponding pole count map in Fig. 1b. This shows how the signature in a pole count map, of stars in a planar orbit, corresponds to a localized peak which coincides with the direction of the normal vector defining the orbital plane.

Since two antiparallel pole vectors define the same plane or great circle in the celestial sphere, the information on one hemisphere of a pole count map is replicated on the other; hence the two peaks at exactly opposite directions in Fig. 1b. Figure 1c shows a map of stars in a localized stellar distribution, with the corresponding pole count map in Fig. 1d. The maxima in pole counts are in this case distributed along a great circle. This happens because all the possible planes which contain both, the localized distribution of stars and the observer at the Galactic Center, have poles which are in turn contained in a specific plane, of which the projection on the sky is the great circle seen in Fig. 1d.

In the GC3 method it is expected that the stars in the Galactic background will contribute a smooth distribution across the entire map, modulated only by the stellar density dependence on position in the sky. The stars in a stream, on the other hand, will contribute only to the cells which coincide best with the stream's orbital plane, creating a local maximum in the pole count distribution.

The GC3 method was used on a C-star survey by Ibata et al. (2001) in order to quantify the statistical significance of a great circle C-star overdensity and to identify it as part of the tidal stream from the Sagittarius (Sgr) dSph galaxy. Later, it was used on 2MASS M-giants by Ibata et al. (2002), on a search for tidal debris in the Galactic Halo. They successfully recovered the Sgr stream but failed to identify any other significant features.

In the following subsections we explore the performance of the original GC3 method by applying it to a simulated, or mock Gaia catalogue (B05). The catalogue includes observational uncertainties and a realistic number of stars in the Galactic background. It illustrates the need to modify the original method in order to reduce the contribution of the Galactic background, and increase its sensitivity to detect lower luminosity tidal streams.

## 2.1 The Mock Gaia Catalogue

The Galactic catalogue from B05 constitutes a random realization of kinematic properties of Milky Way stars in the Galactic disc, bulge and halo, with their corresponding density, velocity, age and color distributions, as well as the appropriate normalization in total luminosity. This resulted in a mock Gaia catalogue containing  $\sim 3.5 \times 10^8$  *observable* Milky Way stars with full phase-space information and observational errors as are expected from Gaia, as well as the error-free quantities for comparison. The two most important aspects to be emphasized about the mock catalogue are the realistic simulation of both the observational errors and the total number of stars that will be observable with Gaia, which will be key issues in determining the applicability of any stream searching method.

## 2.2 GC3 Galactic pole count maps

We restricted the catalogue to stars with  $|b| > 10^\circ$ , in order to avoid the Galactic Plane. The tolerance used in (1) was  $\delta\theta = 5^\circ$  which corresponds to the half-width of each great circle cell and the GC3 pole counts were computed on a  $72 \times 72$  cell grid, uniformly spaced on the surface of the celestial sphere. We chose the tolerance to be slightly less

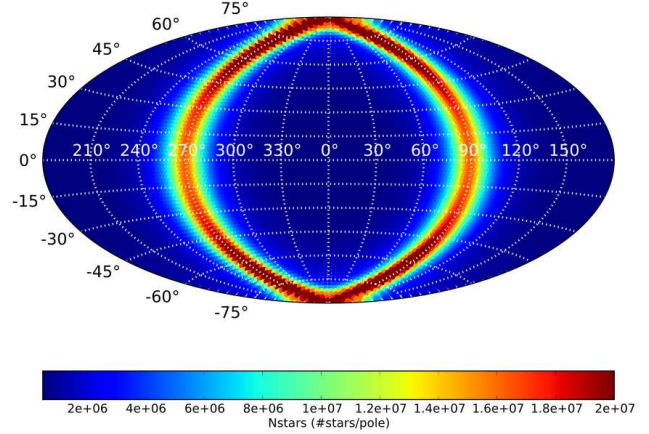


**Figure 2.** GC3 pole count map of Galactic background from error-free mock Gaia catalogue, in a Galactocentric reference frame. The color scale represents the number of stars per pole as shown in the color bar.

than the  $\delta\theta = 6^\circ$  half-width which Ibata et al. (2002) find to maximize the signal to noise ratio of the Sgr tidal stream feature in their 2MASS M-giant pole count maps.

We computed the pole counts for the error-free mock Gaia catalogue, using the GC3 method's position criterion expressed in (1) in a Galactocentric reference frame, i.e. position vectors and pole coordinates are Galactocentric, the latter corresponding to normal vectors of planes that go through the Galactic center. The resulting pole count map is shown in Fig. 2. In this reference frame we name the longitude and latitude angles  $\phi$  and  $\theta$  respectively, with the Galactic Plane at  $\theta = 0^\circ$ , the North Galactic Pole at  $\theta = +90^\circ$  and  $\phi = 0^\circ$  in the direction away from the Sun.

In this reference frame the pole count map would be expected to be uniform in  $\phi$  and with a positive gradient in  $\theta$  (minimum at the equator), because of the axial symmetry of the Galaxy about the Galactic center and the latitude dependence in star density. However, the pole count map shown in Fig. 2 clearly does not follow this pattern in  $\phi$ . This is due to both the exclusion criterion in Galactic latitude ( $|b| > 10^\circ$ ) and the fact we are considering only stars which will be *observable* by Gaia; both criteria being inherently heliocentric. First, the exclusion criterion imposed on the heliocentric Galactic latitude does not filter stars in the Galactic Plane near the Sun at high latitudes, these stars contribute to pole counts for poles in the redish circle in Fig. 2, with their maximum contribution being for  $\phi_{pole} \sim 90^\circ$  and  $\phi_{pole} \sim 270^\circ$ . In addition, planes with  $\phi_{pole} = 0^\circ, 180^\circ$  do not contain solar neighbourhood stars and thus include stars at heliocentric distances that are larger on average than for planes that do go through the Sun with  $\phi_{pole} = 90^\circ, 270^\circ$  (this is illustrated for  $\phi_{pole} \sim 0^\circ$  and  $\phi_{pole} \sim 90^\circ$  in Fig. 3). Therefore the number of observable stars that contribute to poles  $\phi_{pole} \sim 90^\circ, 270^\circ$  will be larger than in the perpendicular direction. These two effects reinforce one another and give rise to the morphology of the pole count map of Fig. 2.

The GC3 method's capability for detecting tidal



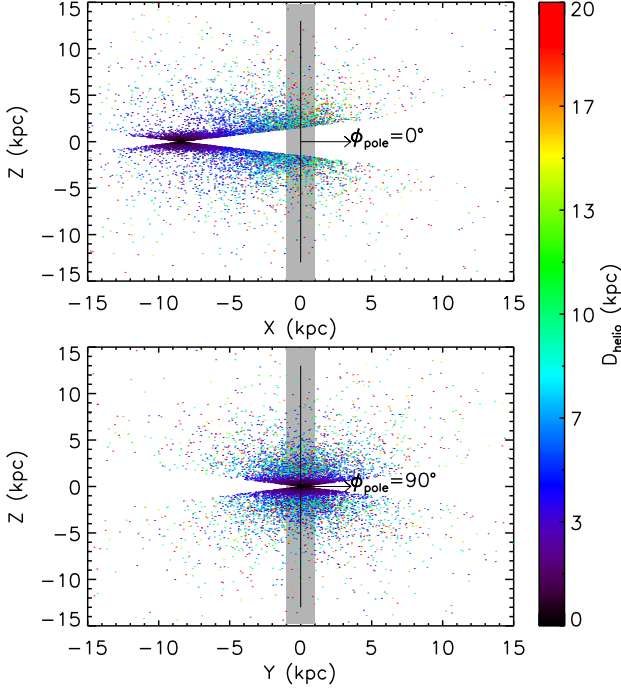


**Figure 3.** Projections of mock Gaia catalogue stars. The color scale indicates heliocentric distances  $D_{\text{helio}}$  as indicated by the color bar. *Top:* X-Z projection. The grey shaded area shows the plane with pole  $\phi_{\text{pole}} = 0^\circ$  and  $\theta = 0^\circ$ , which does not contain solar neighborhood stars. *Bottom:* Y-Z projection. The grey shaded area shows the plane with pole  $\phi_{\text{pole}} = 90^\circ$  and  $\theta = 0^\circ$ . This plane contains solar neighborhood stars. Also, as shown by the color scale, the heliocentric distances of stars in the shaded area of the top panel are on average larger than those in the shaded area in the bottom panel. These effects give rise to the morphology noted on Fig. 2 (see text for details).

streams clearly depends on how large is the contribution of the stream with respect to the Galactic background. In Fig. 2, the mode of pole counts is  $\sim 4.5 \times 10^6$  stars/pole, which is a measure of the typical contribution of Galactic stars in this error-free map. On the other hand, a dwarf galaxy with a stellar population similar to the Galactic Halo (i.e. an age of 13.6 Gyr and iron abundance  $[\text{Fe}/\text{H}] = -1.7$ ) and total luminosity of  $10^7 L_\odot$  has  $\sim 1.2 \times 10^6$  stars brighter than  $M_V = 5$ , according to the stellar population synthesis models of Bruzual & Charlot (2003). The number of *observable* stars, however, will depend on the distance distribution of the stars in the stream, but will necessarily be smaller, specially since most of these are rather faint ( $M_V \gtrsim 4$ ) main-sequence stars. Therefore, the signature of such a dwarf galaxy in a pole count map would be several times below the typical number of Galactic background stars and thus very hard to detect.

As exhibited in this example, the number of Galactic contaminants in a cell is an important limitation of the GC3 method. In the following section we propose a modification of the method, to help discriminate stream stars from the smooth halo using the main attribute of the original GC3 method, namely the use of angular momentum conservation through a geometrical approach.

### 3 THE MODIFIED GC3 METHOD

The GC3 method of Johnston et al., as explained above, uses solely positional information. In order to improve the ‘signal’ of a stellar stream over the ‘noise’ of the smooth background halo population, we propose the inclusion of velocity information as well. Since the stellar stream is roughly confined to a plane that contains the center of symmetry of the potential, as seen from this center both its position and velocity vectors will be contained in the orbital plane.

A grid of all the possible great circle cells is devised, with each cell uniquely determined by its *pole*, that is the unit vector  $\hat{\mathbf{L}}$  which is perpendicular to the plane it defines. The modified GC3 (mGC3) method proposed here for counting the number of stars associated with each pole, can be expressed in terms of the following Galactocentric position and velocity criteria

$$|\hat{\mathbf{L}} \cdot \hat{\mathbf{r}}| \leq \delta_r \quad \text{and} \quad |\hat{\mathbf{L}} \cdot \hat{\mathbf{v}}| \leq \delta_v \quad (2)$$

where  $\hat{\mathbf{r}}$  and  $\hat{\mathbf{v}}$  are unit vectors parallel to the star position and velocity vectors,  $\delta_r$  and  $\delta_v$  are the tolerances which allow for the width of each great circle associated with a cell. The pole vector  $\hat{\mathbf{L}}$  that corresponds to the cell which best coincides with a stream is parallel to the streams’s total angular momentum.

As with the original GC3, the mGC3 criteria in (2) will hold for tidal streams evolved in a spherical or slightly flattened potential. For the Milky Way (MW), according to several authors, the orbit of the Sgr tidal stream constrains the inner halo ( $\lesssim 60\text{kpc}$ ) to be slightly flattened with a Z-axis flattening  $q_z = 0.85 - 0.95$  for oblate models (Johnston, Law & Majewski 2005; Martínez-Delgado et al. 2004; Ibata et al. 2001), and  $q_z = 1.25$  for prolate models (Helmi 2004; Law, Johnston & Majewski 2005); albeit more recently Law, Majewski & Johnston (2009) find that a triaxial halo with  $q_z = 1.25$  and  $q_y = 1.5$  provides a better fit of the radial velocity and distance distribution of observed Sgr stream stars. On the other hand, depending on dynamical age, orbital inclination and how close the stellar system comes to the Galactic plane, the disc’s potential can perturb the symmetry of the overall potential felt by the stream. Johnston et al. (2008) classify stream morphologies resulting from their N-body simulations in three categories ‘great circle’, ‘cloudy’ and ‘mixed’, illustrated in their Fig. 1, as well as transition types in between these categories, as shown in their Fig. 2. The mGC3 criteria proposed here will hold for the ‘great circle’ streams, as well as for the dynamically younger parts of ‘cloudy’ and ‘cloudy-great-circle’ streams, and clearly not for ‘mixed’ morphology streams.

#### 3.1 Practical Implementation of the mGC3 criteria

The position and velocity criteria proposed above, need to be written in terms of observable quantities. Our first step is to write them using the Galactocentric position and velocity vectors of each star:

$$|\hat{\mathbf{L}} \cdot \mathbf{r}_{\text{gal}}| \leq \|\mathbf{r}_{\text{gal}}\| \delta_r \quad \text{and} \quad |\hat{\mathbf{L}} \cdot \mathbf{v}_{\text{gal}}| \leq \|\mathbf{v}_{\text{gal}}\| \delta_v, \quad (3)$$

where  $\delta_r = \sin \delta\psi_r$ ,  $\delta_v = \sin \delta\psi_v$  and  $\delta\psi_r, \delta\psi_v$  are the complements of the angles between  $\hat{\mathbf{L}}$  and the vectors

$\mathbf{r}_{\text{gal}}$ , and  $\mathbf{v}_{\text{gal}}$  respectively, which correspond to the tolerance width of the great circle associated with the cell.

The vectors  $\mathbf{r}_{\text{gal}}$  and  $\mathbf{v}_{\text{gal}}$  are in turn expressed in terms of the observable quantities  $(l, b, \varpi, v_r, \mu_l, \mu_b)$  as follows

$$\begin{aligned} \mathbf{r}_{\text{gal}} &= \mathbf{r}_{\odot} + A_p \varpi^{-1} \left[ (\cos l \cos b) \hat{\mathbf{x}} + (\sin l \cos b) \hat{\mathbf{y}} + (\sin b) \hat{\mathbf{z}} \right] \\ \mathbf{v}_{\text{gal}} &= \mathbf{v}_{\odot} + v_r \hat{\mathbf{r}} + \varpi^{-1} \left[ (A_v \mu_l \cos b) \hat{\mathbf{l}} + (A_v \mu_b) \hat{\mathbf{b}} \right], \end{aligned} \quad (4)$$

where  $A_p = 10^3 \text{ mas-pc}$ ,  $A_v = 4.74047 \text{ yr km s}^{-1}$ ;  $\{\hat{\mathbf{x}}, \hat{\mathbf{y}}, \hat{\mathbf{z}}\}$  are the unit vectors in the cartesian Galactocentric reference frame and  $\{\hat{\mathbf{r}}, \hat{\mathbf{l}}, \hat{\mathbf{b}}\}$  are the unit vectors in a spherical heliocentric reference frame. The latter depend upon  $(l, b)$ , though not on the parallax  $\varpi$ , when expressed in the cartesian Galactocentric reference frame (see Appendix A).

As can be seen from (4), the expressions for the Galactocentric position and velocity vectors  $\mathbf{r}_{\text{gal}}$  and  $\mathbf{v}_{\text{gal}}$  depend upon the reciprocal of the parallax, which as discussed above, will introduce systematic errors in the determination of both vectors. Therefore we define the vectors  $\mathbf{r}'_{\text{gal}} \equiv \varpi \mathbf{r}_{\text{gal}}$ , and  $\mathbf{v}'_{\text{gal}} \equiv \varpi \mathbf{v}_{\text{gal}}$ . With these definitions the parallax will enter multiplying instead of dividing (see 5).

$$\begin{aligned} \mathbf{r}'_{\text{gal}} &= \varpi \mathbf{r}_{\odot} + A_p (\cos l \cos b) \hat{\mathbf{x}} + (\sin l \cos b) \hat{\mathbf{y}} + (\sin b) \hat{\mathbf{z}} \\ \mathbf{v}'_{\text{gal}} &= \varpi \mathbf{v}_{\odot} + \varpi v_r \hat{\mathbf{r}} + (A_v \mu_l \cos b) \hat{\mathbf{l}} + (A_v \mu_b) \hat{\mathbf{b}} \end{aligned} \quad (5)$$

We can thus rewrite the criteria of (3) in terms of the vectors  $\mathbf{r}'_{\text{gal}}$  and  $\mathbf{v}'_{\text{gal}}$  as shown in (6), which will constitute our working criteria.

$$|\hat{\mathbf{L}} \cdot \mathbf{r}'_{\text{gal}}| \leq \|\mathbf{r}'_{\text{gal}}\| \delta_r \quad \text{and} \quad |\hat{\mathbf{L}} \cdot \mathbf{v}'_{\text{gal}}| \leq \|\mathbf{v}'_{\text{gal}}\| \delta_v \quad (6)$$

These expressions are numerically equivalent to those in (3), though they are in practice more useful, since the effect of error propagation due to the reciprocal of the parallax is avoided. The method based on these criteria relies on an accurate knowledge of  $\mathbf{r}_{\odot}$  and  $\mathbf{v}_{\odot}$ , which we can expect to be accurately determined from Gaia data.

### 3.2 Modified GC3 applied to the mock Gaia Catalogue

We computed the pole counts for the mock Gaia catalogue described in Sec. 2.1, now using the modified GC3 (mGC3) criteria expressed in (6). As in Sec. 2, we restricted the catalogue to stars with  $|b| > 10^\circ$  and the mGC3 pole counts were computed on a  $72 \times 72$  cell grid, with equal tolerances for the position and velocity criteria  $\delta\psi_r = \delta\psi_v = 5^\circ$ .

#### 3.2.1 mGC3 pole counts of mock catalogue without errors

For the error-free mock catalogue the resulting pole count map is shown in Fig. 4. In this map the mode of pole counts is  $\sim 4 \times 10^5$ , a factor of 10 lower than the typical pole counts in the GC3 map of Fig. 2. This is a consequence of the velocity requirement of (6), which decreases the overall number of stars per pole because the contribution to any given pole, or great circle cell, does not come from all the stars in the plane of the great circle associated with the cell, but comes only from those whose velocity is also contained in the great circle plane, therefore decreasing the contribution to each pole by chance alignments. This effectively lowers the pole counts on the whole map and also reduces the strength of the pattern of excess pole counts around  $\phi_{\text{pole}} = 90^\circ, 270^\circ$

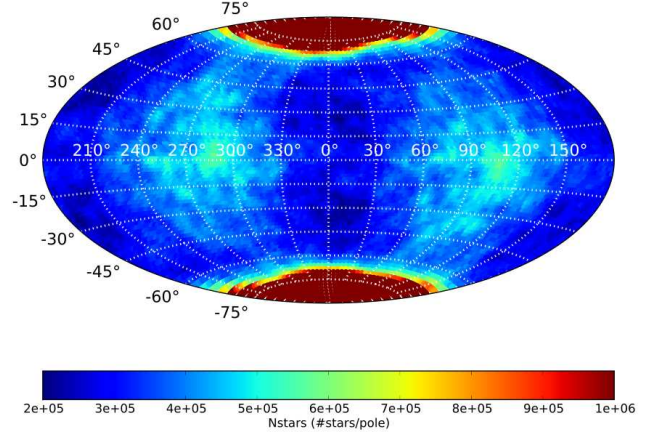


**Figure 4.** Map of mGC3 pole counts for mock Gaia catalogue *without* observational errors. The color scale represents the number of stars per pole as shown in the color bar. Notice the change in normalization with respect to Fig. 2

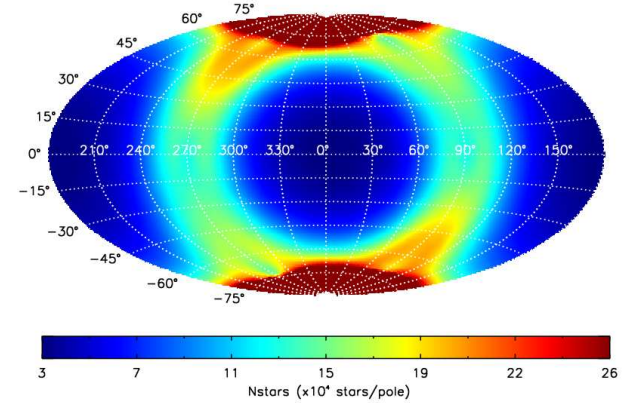


**Figure 5.** Map of mGC3 pole counts for mock Gaia catalogue *including* simulated observational errors. The color scale represents the number of stars per pole as shown in the color bar. Note that the maximum of the color scale in this figure is  $\sim 10$  per cent of Fig. 4.

because, as discussed in Sec. 2, the majority of stars that contribute to this excess are in the Galactic Plane, and so their velocities do not lie on the plane associated to these  $\phi_{\text{pole}}$  values.

#### 3.2.2 mGC3 pole counts of mock catalogue with errors

The pole count map for the mock catalogue *including* the simulated errors is shown in Fig. 5 and was computed using only stars with  $|b| > 10^\circ$  and with positive parallax with errors smaller than 30 per cent.

This requirement on the parallax causes a pattern of excess pole counts for poles at  $\phi_{\text{pole}} \sim 90^\circ, 270^\circ$ , similar to that seen in the GC3 pole count map discussed in Sec. 2. The origin of this pattern is essentially the same as discussed

**Table 1.** Orbital parameters of simulated satellites

Sat ID	Mass ( $\times 10^7 M_\odot$ )	Pericentre (kpc)	Apocentre (kpc)	Inclination angle ( $^\circ$ )
S1	5.6	8.75	105	30
S2	5.6	7.0	60	45
S3	2.8	7.0	80	60
S4	2.8	40	60	25
S5	2.8	3.5	55	45

in Sec. 2, great circle cells with poles  $\phi_{pole} \sim 0^\circ, 180^\circ$  include stars with heliocentric distances that are on average larger than for perpendicular cells; since parallax errors increase with heliocentric distance, this causes less stars to pass the parallax error filter for cells that do not include the Sun, and conversely an excess for cells that do ( $\phi_{pole} \sim 90^\circ, 270^\circ$ ). However, the background level is vastly reduced compared to that of Fig. 2.

#### 4 APPLICABILITY OF THE MGC3 METHOD

We now evaluate the applicability of the *mGC3* method by applying it to pole count maps including the Galactic background from the mock Gaia catalogue described in Sec. 2.1 and tidal streams from N-body simulations also from B05. In the following section we describe the kinematic and photometric characteristics used in our experiments and the morphology of *mGC3* pole count maps is illustrated in detail in Sec. 4.2 for a typical tidal stream.

##### 4.1 Assigning observable properties to simulated satellite streams

We use the simulated satellites from B05 (see paper for details), which are the results of N-body simulations of self-consistent systems with  $10^6$  particles evolved in a rigid axisymmetric Galactic potential. The Galactic potential used was oblate with a flattening in the potential of  $q_{\phi_h} = 0.8$ . The satellites have two different initial masses of  $2.8 \times 10^7 M_\odot$  and  $5.6 \times 10^7 M_\odot$  and different pericentre, apocentre and inclination angles with respect to the Galactic plane, which are summarized in Table 1. The satellite IDs used here (S1-S5) correspond to the Run No. (1-5) used in Table 6 of B05. The resulting orbits are illustrated in Fig. 4 in B05. For each satellite, snapshots of the distribution of N-body particles are available for dynamical ages ranging from 0 to 9.75 Gyr at 0.65 Gyr steps. We use the term *dynamical age* to emphasize this does not refer to the age of the stellar population, but to the elapsed time in the N-body simulation. We take the dynamical age to be zero in the beginning of the N-body simulation, when the satellite is entirely bound.

Embedding the simulated satellite streams in the Galactic background described in Sec. 2.1, requires that we make a realistic simulation of the number of stars that will be observable by Gaia in each of the simulated satellites. This number depends on the total luminosity  $L_V$  of the satellite; on its orbit, which determines the distribution of observer to star distances along the stream; and on its star formation history (SFH), which will determine the luminosity function of the stellar population at any given age.

For our experiments we varied the total luminosity  $L_V$  in the range  $1 \times 10^7 L_\odot$  to  $1 \times 10^9 L_\odot$ . In all cases the luminosity  $L_V$  refers to the total luminosity of the stars in the whole satellite system including the tidal tails, not just the bound core.

For each simulated satellite we assigned two different SFHs, whose properties are described in Table 2. These are termed Halo-type and Carina-type since they have been tailored to resemble the SFHs of the Galactic Halo and Carina dSph satellite, respectively. As can be seen from Table 2, the Halo-type SFH consists of only an old burst with an age of 13 Gyr, with  $[\text{Fe}/\text{H}]$  near the peak of the iron abundance distribution of halo stars ( $[\text{Fe}/\text{H}] = -1.8$ , Prantzos 2009). The Carina-type SFH consists of three separate bursts producing old (13 Gyr), intermediate-age (8 Gyr) and young (3 Gyr) populations, the intermediate and old being the dominant ones, and a single metallicity (although Carina exhibits a range in  $[\text{Fe}/\text{H}]$  from -2.0 to -1.0, see e.g. Carigi & Hernández 2008; Carigi et al. 2002). This choice of SFHs and  $[\text{Fe}/\text{H}]$  does not intend to accurately represent the stellar populations of neither the present-day dSphs nor of the possible halo building-blocks. It only intends to illustrate the performance of the *mGC3* method in the least favorable case (the Halo-type SFH) and a slightly more favorable one (the Carina-type SFH), in terms of the number of stars observable by Gaia.

Using an adaptation of the Bruzual & Charlot (2003) stellar population synthesis software, we generated a random realization of the photometric properties of stars in a system with total luminosity  $L_V$  and a given SFH and age. This is done by selecting the SFH, and metallicity  $Z$  (a metallicity  $Z=0.0004$  corresponds to an iron abundance  $[\text{Fe}/\text{H}] = -1.7$  at a solar  $[\alpha/\text{Fe}]$  ratio). The ages of the stellar populations were fixed at the values given by the SFHs in Table 2, independently of the dynamical age, for all experiments. Luminosities and temperatures are then randomly drawn for as many stars as necessary, until the total luminosity reaches the desired value of  $L_V$ . Since a large number of the stars in the realization will be low-mass stars too faint to be observed, we keep only the photometric information of stars brighter than an arbitrary cutoff at absolute magnitude  $M_V = 5$ . Although we discard these very faint stars, it is important to emphasize that their luminosities *do* contribute to the total luminosity of the system. The magnitude cutoff was chosen at  $M_V = 5$  since it is fainter than the turn-off of a 13.4 Gyr old population of halo-like metallicity ( $M_V = 4$ ). This ensures that the turn-off will be brighter than our cutoff for a population of any given age. Nevertheless, the fraction of these stars that will be observable will be determined by the Gaia magnitude cut-off ( $V < 20$ ). Following this recipe ensures that our random realization accurately represents both the luminosity function of the stars given by the SFH, as well as the total number of stars in a system with total luminosity  $L_V$ .

Finally, we randomly assign the photometric properties generated with this procedure, to the N-body particles of the simulated satellites as explained in Sec. 4.3 in B05, and then compute, using the recipe detailed in Sec. 4.1 in B05, the Galactic longitude, latitude, parallax, radial velocities and proper motions with their corresponding errors, for each simulated satellite star within the completeness limit of Gaia ( $V < 20$ ).

**Table 2.** Star Formation Histories

Name	Age <sup>a</sup> (Gyr)	[Fe/H] (dex)	$L_V$ (per cent)
Halo-type	13	-1.7	100
	13	-1.7	30
Carina-type	8	-1.7	50
	3	-1.7	20

<sup>a</sup> Age of the star formation bursts assigned to simulated dwarf galaxie

## 4.2 Application to a typical stream

In this section we use a typical satellite stream with a chosen dynamical age, luminosity, orbit and SFH in order to explain the morphology of the pole count map and the methodology devised to detect in it the signature produced by the stream. For the present and all following experiments, pole count maps were produced with a  $72 \times 72$  spherically uniform grid, position and velocity tolerances of  $\delta\psi_r = \delta\psi_v = 5^\circ$  and including from the simulated catalogues only those stars with positive parallax with errors less than 30 per cent and with  $|b| > 10^\circ$ , to avoid the Galactic Plane.

For this example we chose satellite S2 at a dynamical age of 5.85 Gyr, with an elongated and inclined orbit, a Carina-type SFH and total luminosity of  $3 \times 10^8 L_\odot$ . The corresponding Galactocentric sky distribution is shown in Fig. 6. The color scale of the figure indicates the particles' Galactocentric distances. The mGC3 pole count map which corresponds to this simulated stream alone is shown in Fig. 7a; and the mGC3 pole count map of this stream embedded in the Galactic background (with errors) described in Sec. 3.2.2, is shown in Fig. 7b. In this figure, the signature of the stream in pole counts is a barely perceptible excess around  $(\phi_{pole}, \theta_{pole}) = (85^\circ, 35^\circ)^1$ . This is the kind of feature we need to detect in pole count maps in an automated fashion, in order to evaluate the method's capabilities to detect tidal streams of various characteristics.

Since the Galactic background leaves a smooth signature in the pole count maps, we can use the standard image processing technique of *unsharp masking* to remove its contribution. Unsharp masking consists in subtracting from the original image a *smoothed* image, in which the value of each pixel corresponds to the median value in its neighbourhood. The subtracted image or, in this case, the subtracted pole count map has a much more uniform background and the contrast of localized excesses is enhanced. The smoothed image, made from the pole count map on Fig. 7b using a neighbourhood of  $5 \times 5$  pixels, is shown in Fig. 7c. The subtracted pole count map is shown in Fig. 7d for the present example. In this subtracted map the stream's signature is much more evident than it was in the original pole count map (Fig. 7b). The color scale in the subtracted map indicates the amplitude or height of the excesses in units of the background's standard deviation  $\sigma$ , and clearly shows that the stream in this example is detected at the  $\sim 7\sigma$  level in

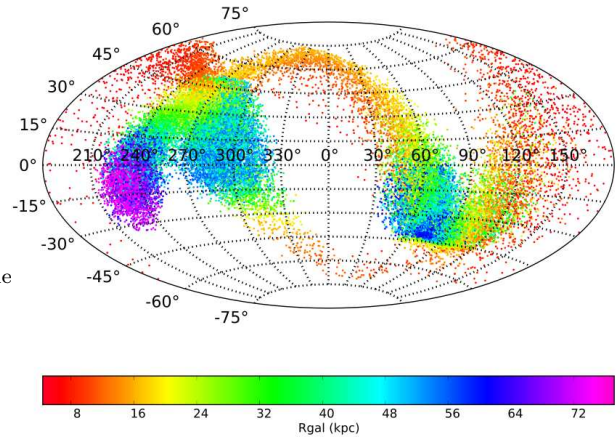


**Figure 6.** Galactocentric sky distribution of N-body particles in satellite S2 at a dynamical age of 5.85 Gyr. The color scale represents Galactocentric distance as shown in the color bar.

the subtracted pole count map; whereas in original map the excess appears only at the  $\sim 2\sigma$  level.

The subtracted pole count map of Fig. 7d still shows signs of non-uniformity. Some regions in the subtracted map, particularly near an excess, appear with pole counts below the background (i.e. negative sigma amplitudes in Fig. 7d). This is caused by an oversubtraction of the background due to the excess itself, which increases the median value of the pole counts in pixels surrounding it in the smoothed image. Also, spurious detections tend to arise at the  $2 - 3.5\sigma$  level due to imperfections in the background subtraction. In the examples of following sections we consider *bona fide* excess detections as those corresponding to excess counts with amplitudes larger than  $4\sigma$ . We also require  $|\theta_{pole}| < 80^\circ$ , consistently with our avoidance zone of  $|b| > 10^\circ$ .

In the following section we systematically apply this procedure to recover the simulated streams from the detection of excesses in mGC3 pole count maps.

## 5 VARIABLES AFFECTING THE DETECTABILITY OF TIDAL STREAMS

In this section we explore the efficiency of the method in recovering simulated streams under different conditions of total luminosity, SFH and orbital parameters.

### 5.1 Total Luminosity and Star Formation History

The effect of increasing the total luminosity  $L_V$  of a system is to increase the number of observable stars proportionally. The stream's signature increases with total luminosity, as can be seen in Fig. 8. For all five satellites, at an arbitrarily fixed dynamical age of 7.15 Gyr, Fig. 8 shows the amplitude of the excesses recovered as a function of  $L_V$ . The signal to noise ratio (SNR, understood as height of the peak over mean background, in terms of the background's  $\sigma$ ) of the stream increases with  $L_V$ . For some satellites, i.e. S2, the

<sup>1</sup> The slight differences in the shape of map features with  $\theta < 0^\circ$  compared to those with  $\theta > 0^\circ$  are an effect of the Aitoff projection.



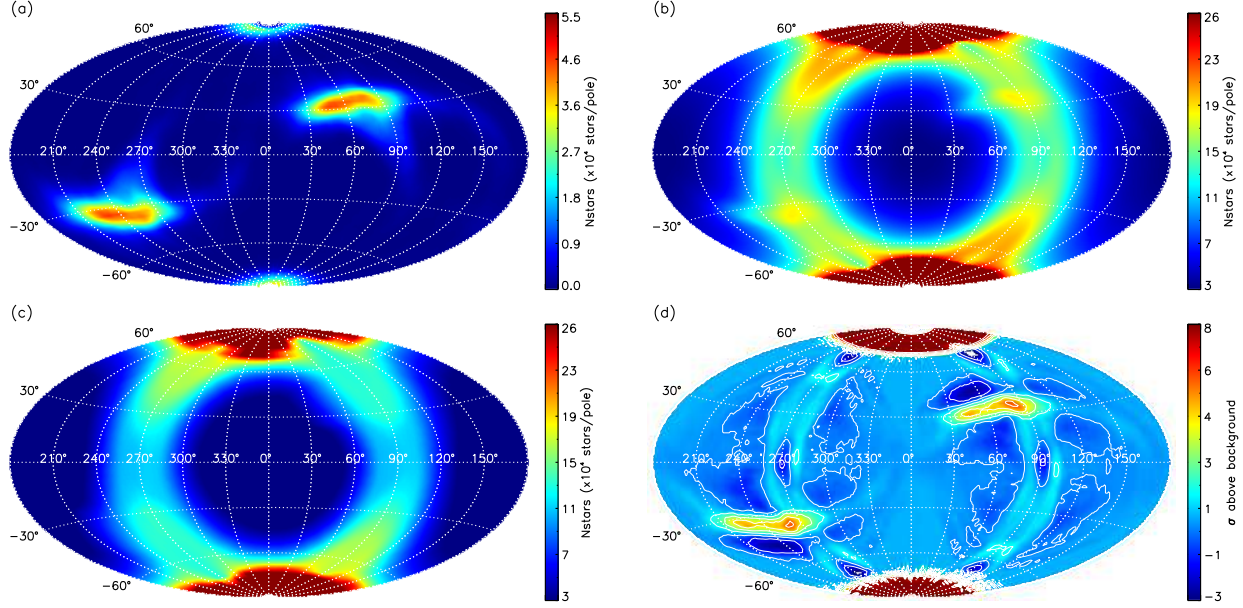


**Figure 7.** (a) Map of *mGC3* pole counts for stars in satellite S2 alone, at a dynamical age of 5.85 Gyr. (b) Map of *mGC3* pole counts for satellite S2 (panel a) embedded in the mock Galactic background. (c) Smoothed image of the pole count map in panel (b) used for the ‘unsharp masking’. The color scales of panels (a), (b) and (c) represent the number of stars per pole as shown in the color bar. Note that the range of the color scale of panel (a) is 5 times smaller than that of panels (b) and (c). (d) Subtracted pole count map. The color scale and contours represent the amplitude or height of the excesses in units of the background’s standard deviation  $\sigma$ .

SNR reaches a plateau since, depending on the shape of the stream, the pole count signature can differ from a localized peak if the stream is very disrupted (see stream orbits in Fig. 4 of B05). Therefore increasing the luminosity can also increase the dispersion of pole counts in the background, maintaining the height approximately constant when expressed in terms of the background’s standard deviation, as in Fig. 8.

Figure 8 also shows the effect of varying the SFH, which in terms of the pole count maps is only reflected in a change in the fraction of observable stars. At the same total luminosity, a SFH having young or intermediate-age bursts (i.e. a Carina-like SFH) yields a larger fraction of brighter stars compared to a population with only an old burst (i.e. an Halo-like SFH). This can be seen in Fig. 8, where for most satellites at a given luminosity a stream is detected at a lower sigma level if the population is given by the Halo-like SFH (triangles) than if it is given by a Carina-like SFH (circles). For very disrupted satellites like S2 and S5, as mentioned before, the signature in pole count maps differs from a localized peak; therefore the significance of the detection saturates earlier in luminosity for brighter populations causing the stream to be detected at higher sigma levels for fainter populations.

Finally, it can be seen that satellite S1 can be detected with the *mGC3* method down to a luminosity as low as  $\sim 4 \times 10^7 L_\odot$ , even for this old dynamical age of 7.15 Gyr.

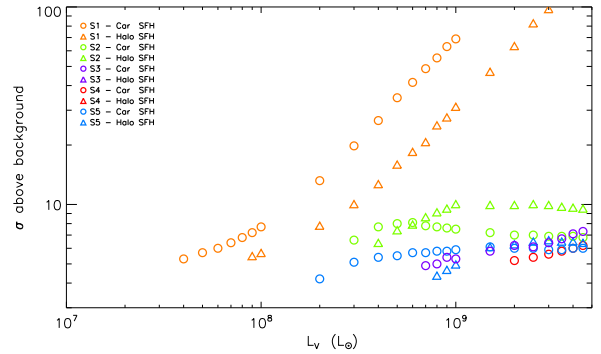


**Figure 8.** Height of detected maxima on pole count maps as a function of the satellite’s initial total luminosity  $L_V$ .

## 5.2 Orbital parameters and dynamical age

Orbital parameters are clearly important since they determine the shape of the orbit. How disrupted the stream will become strongly depends on the perigalacticon and inclination angle. Nevertheless, the most influential parameter affecting the detectability is rather the distribution of heliocentric distances of the stream stars at different dynamical ages, since this will determine the fraction of stars that will be observable in our simulated survey.

For all dynamical ages of the five satellite’s streams, we computed  $D_{\text{helio}}$  the mean of the heliocentric distance distribution, as a measure of a representative heliocentric distance of the system. The plot of  $D_{\text{helio}}$  as a function of

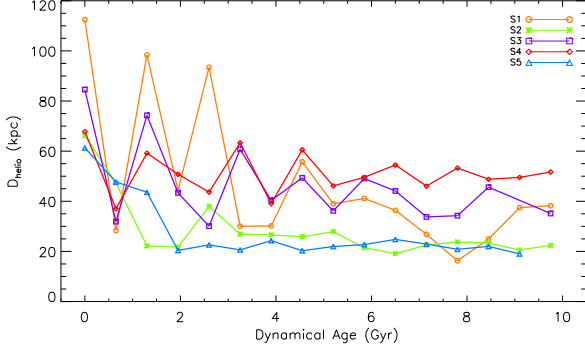


**Figure 9.** Heliocentric distance  $D_{\text{helio}}$  as a function of dynamical age for all five satellites.

dynamical age in Fig. 9, shows that as the dynamical age increases, stream stars can come closer to the Sun as they are gradually distributed along the orbit, hence decreasing the mean of the distribution of  $D_{\text{helio}}$ . This effect would be enhanced by the action of dynamical friction which, although not included in the simulations, is expected to contribute in the evolution of real systems.

Therefore, the detectability of streams should increase with decreasing  $D_{\text{helio}}$ . This is illustrated in Fig. 10, a plot of the  $\sigma$  detection level of the simulated satellite streams in pole count maps, as a function of  $D_{\text{helio}}$ , for satellites with a Carina-type SFH and two different luminosities  $L_V = 2 \times 10^8 L_\odot$  (bottom) and  $L_V = 2 \times 10^9 L_\odot$  (top). These plots show that old streams ( $\gtrsim 7$  Gyr) at heliocentric distances up to  $D_{\text{helio}} \sim 30$  kpc and  $D_{\text{helio}} \sim 40$  kpc can be detected at a high sigma level, for the bright ( $L_V = 2 \times 10^9 L_\odot$ ) and faint satellites ( $L_V = 2 \times 10^8 L_\odot$ ) respectively. On the other hand, streams can be detected at larger distances only if there's a dynamically younger and/or brighter population. Also, at a given distance, streams with different dynamical ages (color scale) can be detected at different sigma levels.

### 5.3 Combined Effects

In order to combine the different effects that impact the detectability of simulated streams, explored individually in the previous sections, we show in Fig. 11 a plot of the total luminosity  $L_V$  of detectable satellites as a function of  $D_{\text{helio}}$ , for all five simulated satellites at dynamical ages larger than 4.5 Gyr and with Halo-type (*bottom*) and Carina-type (*top*) SFHs. This plot shows how all five satellites (S1-S5), which have stars observable by Gaia (and meeting our criteria  $\sigma\omega/\omega \leq 30$  per cent), can be recovered using mGC3 at different dynamical ages, for total luminosities in the range  $10^8 - 10^9 L_\odot$  with both SFHs and even down to  $4 - 5 \times 10^7 L_\odot$  for satellites including a younger stellar population (Carina-type SFH) for certain combinations of dynamical ages and orbital parameters.

A statistical description of the efficiency of the mGC3 method would require a more thorough exploration of the orbital parameter space, but in the present experiments we have only 5 different orbital parameter sets. Nevertheless, these experiments are useful for a first rough exploration of the applicability of the mGC3 method in which, as shown

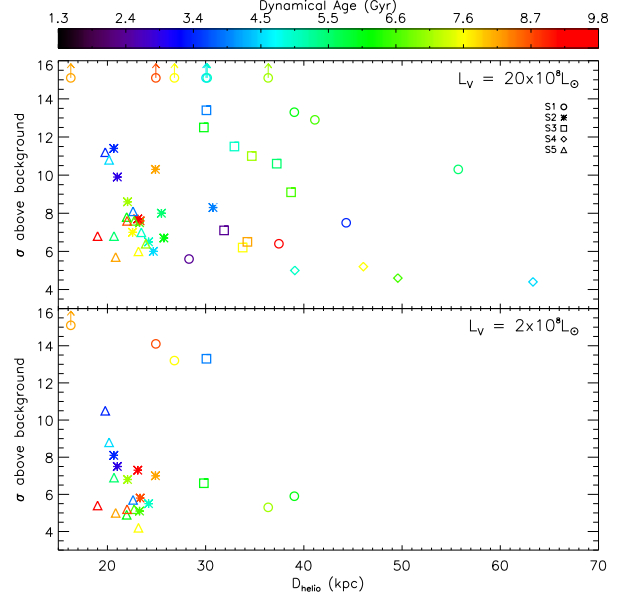


**Figure 10.** Height of detected excesses on subtracted pole count maps as a function of  $D_{\text{helio}}$ . Satellites have a Carina-type SFH and total luminosities  $L_V = 2 \times 10^8 L_\odot$  (*Bottom*) and  $L_V = 2 \times 10^9 L_\odot$  (*Top*). Detections with  $\sigma > 15$  are indicated with upward pointing arrows. The color scale represents dynamical age as shown by the color bar.

in Secs. 5.1 and 5.2, we find that satellites with total luminosities as faint as  $\sim 5 \times 10^7 L_\odot$ , or as dynamically old as  $\sim 9$  Gyr, with different orbital parameters, can be recovered. Furthermore, the experiments carried out illustrate a lower limit on the capabilities of the mGC3 method, since in our simulations we use *only* the information from trigonometric parallaxes to obtain the distances to stars. Gaia, however, will also provide *photometric* parallaxes for a much larger, fainter and more distant sample of stars, than those for which trigonometric parallaxes can be measured accurately.

## 6 DISCUSSION AND CONCLUSIONS

Motivated by the desire to unravel the fossil record of the formation of our Galaxy we have developed an extension of the GC3 method of Johnston et al. (1996) in order to apply this to the search for satellite remnants in the Galactic halo. The GC3 method is essentially a means of grouping together stars on the sky with the same orbital angular momentum, thus identifying stars along the same Great Circle. The original method suffers from a strong contaminating background in the pole count maps as demonstrated in Section 3. These background counts are due to the general Galactic population of stars and can be much reduced by adding a kinematic criterion to the search for stars with similar orbital angular momenta. This constitutes the extended mGC3 method presented in this paper.

We applied this new method to a mock Gaia catalogue containing some  $3.5 \times 10^8$  stars that form the smooth Galactic background and stars from simulated satellite galaxies on

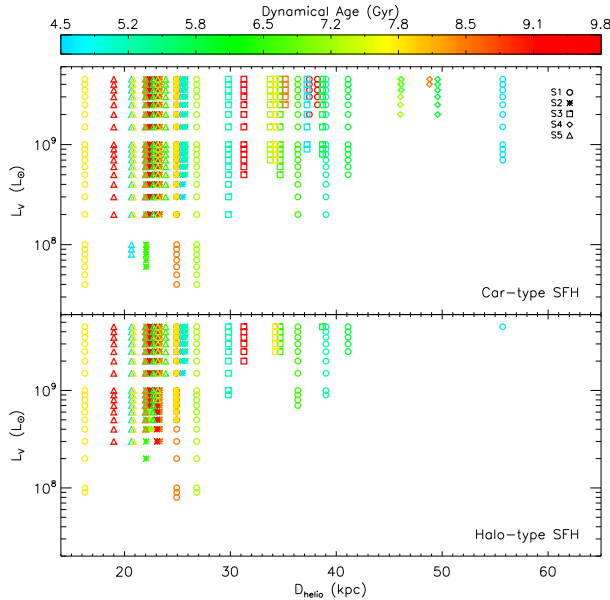


**Figure 11.** Total luminosity  $L_V$  of detectable satellites as a function of the heliocentric distance, for dynamical ages greater than 4.5 Gyr, assuming a Halo-type SFH (*bottom*) and a Carina-type SFH (*top*). The color scale represents dynamical age as shown by the color bar.

different orbits and with two types of star formation histories. The results show that the mGC3 method is capable of tracing remnants of satellites with luminosities down to  $L_V \sim 4 - 5 \times 10^7 L_\odot$  for dynamical ages up to  $\sim 7$  Gyr. Remnants of brighter satellites ( $10^8 - 10^9 L_\odot$ ) can be recovered up to dynamical ages of  $\sim 10$  Gyr. The method works well for most satellites out to a heliocentric distance of 40 kpc. At larger distances only the brightest and/or dynamically youngest satellites can be recovered.

Like the original GC3 method our extended version is limited to recovering remnants of satellites of which the orbits are broadly confined to a plane. This makes this method well suited for probing the outer halo of our Galaxy where the potential is more nearly spherical or axisymmetric and where dynamical timescales are long. The mGC3 method thus forms an important complement to the phase space structure characterization methods which will be used in the inner halo, where due to the short dynamical timescales phase space substructures are harder to detect. In these regions it will be mandatory to use very accurate measurements of integrals of motion employing methods such as those as proposed in Helmi & de Zeeuw (2000) and Gómez & Helmi (2010). In both cases only the use of the highest accuracy parallaxes (relative errors better than about 10 per cent, see also Gómez et al. 2010) allows the recovery of phase space substructure. In contrast the mGC3 method works with 30 per cent accurate parallax data making it suitable for probing larger distances.

The Gaia mission is expected to map the immediate Solar neighbourhood to very high accuracy resulting in some 10 million stars with distances known to better than a few per cent. This will enable a much more accurate calibration of other distance indicators, in particular photometric indi-

cators, which can then be used to extend the mGC3 method also to large samples beyond 40 kpc. In addition the Gaia mission will result in a first order smooth dynamical model of the Milky Way Galaxy which can be used to construct an accurate map of the background mGC3 pole count map. Subtracting a more accurate background map will further enhance the efficiency of the mGC3 method.

We note here two lines of investigation that should be pursued to further investigate and enhance the mGC3 method. (i) The efficiency of the mGC3 method should be explored more extensively by more widely sampling the satellite orbital parameter space. More precise limits on the orbital morphologies and dynamical ages, for which satellites remnants can still be recovered, can then be obtained. In addition, the simulation of the satellites could be made more sophisticated by following the suggestions made in the conclusions of B05. (ii) In connection with these studies it is interesting to investigate to what extent the requirement of single peaks in the pole count map for identifying remnants can be relaxed. This would enable us to account for the precession of the orbital angular momentum vector and thereby recover a larger fraction of the stellar population of a given disrupted satellite. A hint of this possibility can already be seen in the double peaked structure of the signature of the satellite S2 in the map presented in Fig.7.

Finally, the mGC3 method is not perfect and will certainly pick up stars from the field population that appear to belong to a satellite because they are measured to have a compatible orbital angular momentum vector. These should be weeded out by making use of the fact that the different star formation histories for the different satellites will lead to different abundance patterns in their stellar populations. Gross distinctions (such as large overall metallicity differences) can be made photometrically. However, eventually the stars identified as part of a potential satellite remnant should be targeted for detailed spectroscopic follow up in order to definitively ‘tag’ the stars to their progenitor galaxy and obtain accurate information on the progenitor’s time of accretion.

We look forward the time ahead of us when, thanks to the Gaia mission, complementary spectroscopic data, and efficient methods of characterizing substructure in phase space, we will enter the era of precision Galactic archaeology.

We acknowledge support from CONACyT-México grant 60354. C. Mateu acknowledges support from the predoctoral grant of the Academia Nacional de Ciencias Físicas, Matemáticas y Naturales of Venezuela.

## REFERENCES

- Abadi M. G., Navarro J. F., Steinmetz M., Eke V. R. 2003, *ApJ*, 591, 499
- Antoja T., Valenzuela O., Pichardo B., Moreno E., Figueras F., Fernández D., 2009, *ApJL*, 700, L78
- Avila-Reese V., 2006, *arXiv:astro-ph/0605212*
- Bauer A. E., Drory N., Hill G. J., Feulner G., 2005, *ApJL*, 621, L89
- Baugh C. M., 2006, *Reports on Progress in Physics*, 69, 3101
- Belokurov V., Zucker D. B., Evans N. W., Wilkinson M.

- I., Irwin M. J., Hodgkin S., Bramich D. M., Irwin J. M., Gilmore G., Willman B., et al., 2006, *ApJL*, 647, L111
- Brown A. G. A., Velázquez H. M., Aguilar L. A., 2005, *MNRAS*, 359, 1287 (B05)
- Bruzual G., Charlot S., 2003, *MNRAS*, 344, 1000
- Bullock J. S., Johnston K. V., 2005, *ApJ*, 635, 931
- Carigi, L., Hernandez, X., 2008, *MNRAS*, 390, 582
- Carigi, L., Hernandez, X., Gilmore, G., 2002, *MNRAS*, 334, 117
- Colin P., Avila-Reese V., Vazquez-Semadeni E., Valenzuela O., Ceverino D., 2009, *arXiv:0912.4298*
- Cooper A. P., et al., 2009, *arXiv:0910.3211*
- de Blok W. J. G., 2010, *Advances in Astronomy*, 2010,
- De Lucia G., Helmi A., 2008, *MNRAS*, 391, 14
- Diemand J., Madau P., Moore B., 2005, *MNRAS*, 364, 367
- Eggen O. J., Lynden-Bell D., Sandage A. R., 1962, *ApJ*, 136, 748
- Firmani C., Avila-Reese V., Rodriguez-Puebla A., 2009, *arXiv:0909.5188*
- Font A. S., Johnston K. V., Bullock J. S., Robertson B. E., 2006, *ApJ*, 638, 585
- Freeman K., Bland-Hawthorn J., 2002, *ARAA*, 40, 487
- Gentile G., Salucci P., Klein U., Vergani D., Kalberla P., 2004, *MNRAS*, 351, 903
- Gómez F. A., Helmi A., 2010, *MNRAS*, 401, 2285
- Gómez F. A., Helmi A., Brown, A. G. A., 2010, submitted to *MNRAS*, *arXiv:1004.4974*
- Governato F., et al., 2010, *Nat*, 463, 203
- Governato F., Mayer L., Wadsley J., Gardner J. P., Willman B., Hayashi E., Quinn T., Stadel J., Lake G., 2004, *ApJ*, 607, 68
- Governato F., Willman B., Mayer L., Brooks A., Stinson G., Valenzuela O., Wadsley J., Quinn T., 2007, *MNRAS*, 374, 1479
- Helmi A., 2004, *ApJ*, 610, 97
- Helmi A., 2008, *ARA&A*, 15, 145
- Helmi A., de Zeeuw T., 2000, *MNRAS*, 319, 657
- Helmi A., White S. D. M., 1999, *MNRAS*, 307, 495
- Ibata R., Lewis G. F., Irwin M., Totten E., Quinn T., 2001, *ApJ*, 551, 294
- Ibata R. A., Lewis G. F., Irwin M. J., Cambrésy L., 2002, *MNRAS*, 332, 921
- Johnston K. V., Hernquist L., Bolte M., 1996, *ApJ*, 465, 278
- Johnston K. V., Law D. R., Majewski S. R., 2005, *ApJ*, 619, 800
- Johnston K. V., Bullock J. S., Sharma S., Font A., Robertson B., Leitner S. N., 2008, *ApJ*, 689, 936
- Klypin A., Kravtsov A. V., Valenzuela O., Prada F., 1999, *ApJ*, 522, 82
- Klypin A., Trujillo-Gomez S., Primack J., 2010, *arXiv:1002.3660*
- Kravtsov A., 2010, *AdAst*, 2010,
- Koposov S., et al., 2008, *ApJ*, 686, 279
- Law D. R., Johnston K. V., Majewski S. R., 2005, *ApJ*, 619, 807
- Law D. R., Majewski S. R., Johnston K. V., 2009, *ApJ*, 703 L67
- Lindgren L., Babusiaux C., Bailer-Jones C., Bastian U., Brown A.G.A., Cropper M., Høg E., Jordi C., Katz D., van Leeuwen F., Luri X., Mignard F., de Bruijne J., Prusti T., 2008, *IAUS*, 248, 217
- Martínez-Delgado D., Gómez-Flechoso M. A., Aparicio A., Carrera R., 2004, *ApJ*, 601, 242
- Minchev I., Quillen A. C., Williams M., Freeman K. C., Nordhaus J., Siebert A., Bienaymé O., 2009, *MNRAS*, 396, L56
- Moore B., Ghigna S., Governato F., Lake G., Quinn T., Stadel J., Tozzi P., 1999, *ApJL*, 524, L19
- Okamoto T., Eke V. R., Frenk C. S., Jenkins A., 2005, *MNRAS*, 363, 1299
- Prantzos N., 2009, *IAUS*, 254, 381
- Puglielli D., Widrow L. M., Courteau S., 2010, *arXiv:1002.0819*
- Robertson B., Bullock J. S., Font A. S., Johnston K. V., Hernquist L., 2005, *ApJ*, 632, 872
- Searle L., Zinn R., 1978, *ApJ*, 225, 357
- Simon J. D., Geha M., 2007, *ApJ*, 670, 313
- Spergel D. N., et al., 2007, *ApJS*, 170, 377
- Springel V., Frenk C. S., White S. D. M., 2006, *Nat*, 440, 1137
- Steinmetz M., Zwitter T., Siebert A., Watson F. G., Freeman K. C., et al., 2006, *AJ*, 132, 1645
- Tolstoy E., Hill V., Tosi M., 2009, *ARAA*, 47, 371
- Valenzuela O., Rhee G., Klypin A., Governato F., Stinson G., Quinn T., Wadsley J., 2007, *ApJ*, 657, 773
- Yanny B., et al., 2009, *AJ*, 137, 4377
- Zolotov A., Willman B., Brooks A. M., Governato F., Brook C. B., Hogg D. W., Quinn T., Stinson G., 2009, *ApJ*, 702, 1058

## APPENDIX A: COORDINATE TRANSFORMATIONS

In the following we describe the coordinate transformation involved in expressing Galactocentric position  $\mathbf{r}_{\text{gal}}$  and velocity  $\mathbf{v}_{\text{gal}}$  in terms of the heliocentric observable quantities  $(l, b, \varpi, v_r, \mu_l, \mu_b)$ , latitude, longitude, parallax, radial velocities and proper motions respectively.

The Galactocentric position and velocity are expressed as

$$\begin{aligned}\mathbf{r}_{\text{gal}} &= \mathbf{r}_{\odot} + A_p \varpi^{-1} \hat{\mathbf{r}} \\ \mathbf{v}_{\text{gal}} &= \mathbf{v}_{\odot} + v_r \hat{\mathbf{r}} + \varpi^{-1} \left[ (A_v \mu_l \cos b) \hat{\mathbf{l}} + (A_v \mu_b) \hat{\mathbf{b}} \right]\end{aligned}\quad (\text{A1})$$

where  $A_p = 1000 \text{ mas}\cdot\text{pc}$ ,  $A_v = 4.74047 \text{ yr km s}^{-1}$  and  $\{\hat{\mathbf{r}}, \hat{\mathbf{l}}, \hat{\mathbf{b}}\}$  are the unit vectors in a spherical heliocentric reference frame. The latter are expressed in terms of the unit vectors in the cartesian heliocentric reference frame  $\{\hat{\mathbf{x}}, \hat{\mathbf{y}}, \hat{\mathbf{z}}\}$  as follows

$$\begin{aligned}\hat{\mathbf{r}} &= (\cos l \cos b) \hat{\mathbf{x}} + (\sin l \cos b) \hat{\mathbf{y}} + (\sin b) \hat{\mathbf{z}} \\ \hat{\mathbf{l}} &= -(\sin l) \hat{\mathbf{x}} + (\cos l) \hat{\mathbf{y}} \\ \hat{\mathbf{b}} &= -(\sin b \cos l) \hat{\mathbf{x}} - (\sin b \sin l) \hat{\mathbf{y}} + (\cos b) \hat{\mathbf{z}}\end{aligned}\quad (\text{A2})$$

where  $\hat{\mathbf{x}}$  points from the Sun in the GC-Sun direction,  $\hat{\mathbf{y}}$  points in the direction of Galactic rotation and  $\hat{\mathbf{z}}$  points towards the North Galactic Pole. The relative orientation of the unit vectors in both reference frames is shown in Figure A1.

Finally,  $\mathbf{r}_{\text{gal}}$  and  $\mathbf{v}_{\text{gal}}$  are



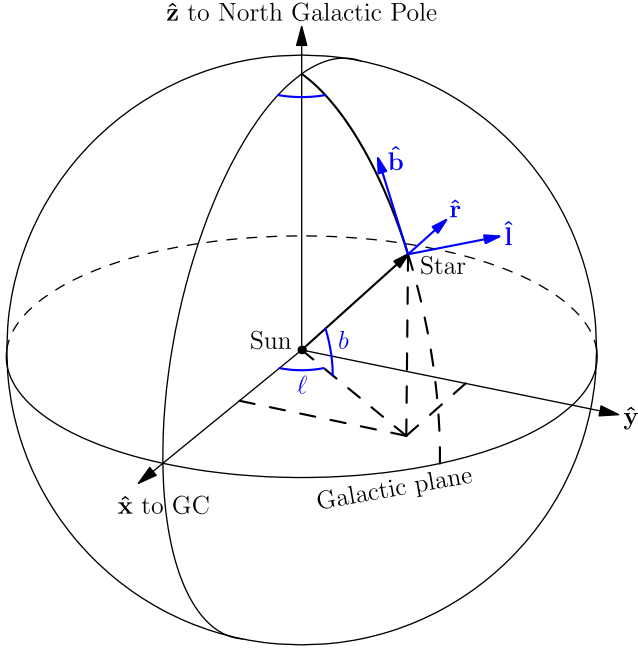


**Figure A1.** Relative orientation of the unit vectors  $\{\hat{\mathbf{r}}, \hat{\mathbf{l}}, \hat{\mathbf{b}}\}$  and  $\{\hat{\mathbf{x}}, \hat{\mathbf{y}}, \hat{\mathbf{z}}\}$ , which respectively define the spherical heliocentric and cartesian Galactocentric reference frames used.

$$\begin{aligned}
 \mathbf{r}_{\text{gal}} &= \mathbf{r}_{\odot} + A_p \varpi^{-1} [(\cos l \cos b) \hat{\mathbf{x}} + (\sin l \cos b) \hat{\mathbf{y}} + (\sin b) \hat{\mathbf{z}}] \\
 \mathbf{v}_{\text{gal}} &= \mathbf{v}_{\odot} + [v_r \sin b + A_v \varpi^{-1} \mu_b \cos b] \hat{\mathbf{z}} \\
 &\quad + [v_r \cos l \cos b - A_v \varpi^{-1} (\mu_l \cos b \sin l + \mu_b \sin b \cos l)] \hat{\mathbf{x}} \\
 &\quad + [v_r \sin l \cos b + A_v \varpi^{-1} (\mu_l \cos b \cos l - \mu_b \sin b \sin l)] \hat{\mathbf{y}}
 \end{aligned}$$

As can be seen from these equations,  $\mathbf{r}_{\text{gal}}$  and  $\mathbf{v}_{\text{gal}}$  depend upon  $(l, b)$  and the reciprocal of the parallax  $\varpi$ , as noted in Section 3.1.